Library-Based Illumination Synthesis for Critical CMOS Patterning

Jue-Chin Yu, Peichen Yu, and Hsueh-Yung Chao

Abstract—In optical microlithography, the illumination source for critical complementary metal–oxide–semiconductor layers needs to be determined in the early stage of a technology node with very limited design information, leading to simple binary shapes. Recently, the availability of freeform sources permits us to increase pattern fidelity and relax mask complexities with minimal insertion risks to the current manufacturing flow. However, source optimization across many patterns is often treated as a design-of-experiments problem, which may not fully exploit the benefits of a freeform source. In this paper, a rigorous source-optimization algorithm is presented via linear superposition of optimal sources for pre-selected patterns. We show that analytical solutions are made possible by using Hopkins formulation and quadratic programming. The algorithm allows synthesized illumination to be linked with assorted pattern libraries, which has a direct impact on design rule studies for early planning and design automation for full wafer optimization.

Index Terms—Inverse lithography, objective function, optical lithography, segment-based optical proximity correction (OPC), source mask optimization (SMO), source synthesis.

I. INTRODUCTION

WITH the advent of immersion and various reticle enhancement techniques, the 193 nm optical lithography has been pushed to a front where critical patterns can be developed well below the Rayleigh resolution limit in low-k1 systems [1]. To further stretch the Moore's law, various resolution enhancement technologies (RET) have been extensively investigated over the last decade, including inverse mask design [2]–[10], multi-mask patterning [11]–[13], iterative source-mask optimization (SMO) [14]–[31], etc. More general reviews and discussions of RET can be found in [32]–[37]. While these technologies are very appealing to semiconductor industry, their insertion into current manufacturing nodes still faces tremendous challenges in terms of flow validation, reticle manufacturing, and computational cost. Most important of all, since the applications of these RETs take place after the design

layout has been created, issues related to patterning cannot be fed back early to prevent problems in advance. As a result, possibilities of design-for-manufacturing desired for advanced CMOS nodes have been overlooked.

At the beginning phase of a technology node planning, a patterning team investigates potential photoresists and illumination modes on various isolated and nested patterns in order to determine reasonable critical dimensions (CDs) for each layer. The collected scanning electron microscopy (SEM) data with corresponding illumination sources are made into preliminary optical proximity correction (OPC) models for generating recipes for test vehicles, normally including bit cells and some random logics. It is at this stage that the design and patterning teams interact heavily to determine the design rules based on the learning from previous technologies. However, restricted design rules alone are not sufficient to make progressively shrunken CDs nowadays. Therefore, the placement of sub-resolution assist features on reticles and double patterning techniques, also known as coloring are demanded to open up the process window at the cost of mask manufacturing.

On the other hand, a well customized illumination source allows a much improved process margin and pattern fidelity without stringent design rules and aggressive OPC [21]. Although off-axis illumination in conjunction with gridded design has been used since last decade, freeform sources are recently made available based on micro-electrical-mechanical mirrors and diffraction optical elements (DOE) [25]. In other words, despite the insertion of a free form source has minimal auxiliary effects to current manufacturing flow and can occur early for technology node planning, the strategies of source optimization (SO) have not been openly discussed. Considering the critical features for patterning are usually scattered in different functional blocks, such as standard cells, synthesized logic, and memory cells, the source optimized for individual critical feature will favor random or repetitive patterns, but not both. Since it can be proved by set theory that only critical patterns and critical combinations of patterns determine the final optimal source and mask [24], many studies therefore adopt a divide-and-conquer approach to prioritize the critical patterns for optimization [22], [23].

From this point of view, we propose a library-based concept for optimal illumination synthesis. The optimal sources for individual critical patterns are first calculated and stored in a library. Through a linear combination of the library sources, we show that the optimal source can be solved exactly using Hopkins formulation and a conjugate gradient (CG) algorithm.
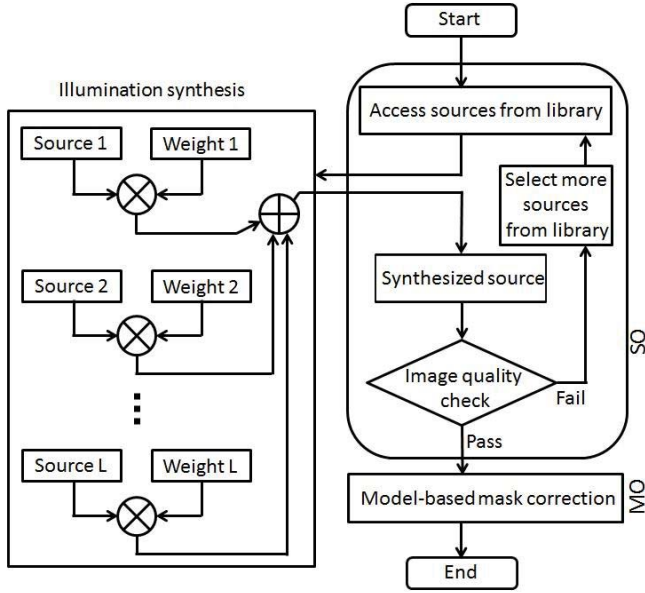
Fig. 1. Flowchart demonstrating how the library-based illumination synthesis fits in a single-pass SMO, where L is the number of sources for illumination synthesis.

Fig. 2. Flowchart demonstrating how the synthesized source computed in Fig. 1 can be fed as an initial guess to iterative SMO.

A critical design of this algorithm relies on the objective functions that formulate SO into a quadratic programming problem, instead of nonlinear programming. The weighting coefficients in the source superposition can then be computed exactly by incorporating the decomposed kernels of pre-stored sources using Hopkins formulation. Such computation is not time-consuming because the kernels of pre-stored sources are generated prior for caching. Therefore, the synthesized illumination can be used for the subsequent mask optimization (MO) (Fig. 1) or fed to iterative SMO as an initial guess (Fig. 2).

Moreover, it has come to our realization during this paper that a fully optimized illumination offers a unique capability to shift the complexity of inverse design from masks to sources. In other words, the novel concepts are fully compatible with existing RET options by relieving the intensive OPC/SRAF requirement and can significantly reduce the computational cost of SMO for full-chip optimization. Furthermore, by linking with the standard cell library and bit cells, the illumination synthesis algorithm also shows potential to plan design rules and determine optimal sources during early exploration of technology nodes.

In Section II, we first review the formulation of image formation using Abbe's method, followed by the definition of objective functions and the search of the optimized source by a conjugate gradient algorithm. Next, the optimal sources obtained for sub-masks are used as the basis of superposition for synthesized illumination. Then a model-based OPC is introduced as a means to evaluate the performance of the synthesized illumination. Section III first demonstrates the advantages of an optimal freeform source over the conventional dipole binary source for a vertical line array with a challenging critical dimension (CD). Next, library-based synthesis of three sub-masks is performed and compared to
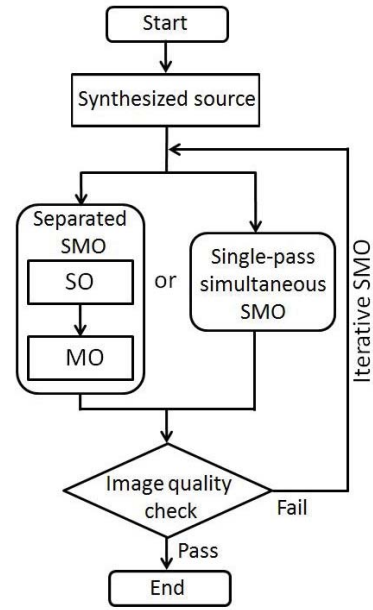
an optimized conventional annular source in terms of image quality and process variation at critical locations. Finally, the benefits of the proposed library-based illumination synthesis are summarized.

II. FORMULATION

A. Image Formation by Source Integration–Abbe's Method

The lithography image or so-called aerial image represents the optical intensity distribution formed by the projection system on the coated wafer. It can be simulated by Abbe's method [34], [38] which integrates the images formed by all source points incoherently

$$
I(x, y) = \int\int_{-\infty}^{\infty} J(f, g)
$$
$$
\times \left[\left| \int\int_{-\infty}^{\infty} H(f+f', g+g') M(f', g') e^{-i2\pi[f'x+g'y]} df' dg' \right|^2 \right] df dg
$$

$$(1)$$

where (x, y) and (f, g) denote the spatial coordinates and spatial frequencies of mask, respectively. $J(f, g)$ is the strength of the point source located at (f, g) [34]. $H(f, g)$ is the optical system transfer function and $M(f, g)$ is the mask spectrum.

Since the optical system is band-limited [39], the transfer function $H(f, g)$ can be described by a low-pass filter

$$
\begin{cases} H(f, g) = 1, & \sqrt{f^2 + g^2} \le \frac{NA}{\lambda}, \\ H(f, g) = 0, & \text{otherwise} \end{cases}
$$

$$(2)$$

where NA is the numerical aperture which limits the largest oblique angle of rays forming the aerial image, λ is the working wavelength, and NA/λ represents the cut-off frequency of the optical system.

In a partially coherent system, the finite source $J(f, g)$ is limited by the coherent factor σ $(0 \leq \sigma \leq 1)$ [34], [35]

$$
\begin{cases}
J(f, g) \geq 0, & \sqrt{f^2 + g^2} \leq \sigma \frac{NA}{\lambda}, \\
J(f, g) = 0, & \text{otherwise.}
\end{cases}
\tag{3}
$$

The spectral integral in the bracket of Eq. (1) is defined as the illumination-cross coefficient (ICC) [40], [42]

$$
ICC(x, y; f, g) =
$$

$$
\left| \int\int_{-\infty}^{\infty} H(f + f', g + g')M(f', g')e^{-i2\pi[f'x+g'y]}df'dg' \right|^2.
\tag{4}
$$

B. Discretization and Objective Functions

Because ICC represents the image formed by a unit source with spatial frequencies (f, g), Eq. (1) can be interpreted as a linear superposition of images with coefficients $J(f, g)$. For computing pixelated images, Eq. (1) is discretized as

$$
I(i, j) = \sum_{k=1}^{O} \sum_{l=1}^{O} J(k, l)ICC(i, j; k, l), \quad i, j = 1, 2, \ldots, N \tag{5}
$$

where the variables $i, j, k,$ and l denote the indices of discretized $x, y, f,$ and g, respectively; N and O are the total sample numbers in spatial and spectral domains. Likewise the ICC in Eq. (4) can be discretized as

$$
ICC(i, j; k, l) = \left| \sum_{k'} \sum_{l'} H(O - [O/2]_{Int} - k + k', \right.
$$

$$
\left. O - [O/2]_{Int} - l + l')M(k', l')e^{-i2\pi[f(k'l')x(i,j)+g(k',l')y(i,j)]} \right|^2.
\tag{6}
$$

k' and l' are both positive indexes where $\max(1, [O/2]_{Int} + k + 1 - O) \leq k' \leq \min([O/2]_{Int} + k, O)$ and $\max(1, [O/2]_{Int} + l + 1 - O) \leq l' \leq \min([O/2]_{Int} + l, O)$. $[O/2]_{Int}$ denotes the maximum integer smaller than $O/2$.

In order to find the optimal source, the proper objective functions for quantifying the deviation between ideal design and real simulation should first be defined. By incorporating the weight function ω that spatially filters the feasible image parts, SO is turned into a linear least squares (LLS) problem [19]. Therefore, the overall objective function $F_{Overall}$ can be written as

$$
F_{Overall} = \sum_{i}^{N} \sum_{j}^{N} (\omega(I - \Gamma))^2(i, j)
$$

$$
= \sum_{i}^{N} \sum_{j}^{N} \left(\sum_{k}^{O} \sum_{l}^{O} [\omega(i, j)ICC(i, j; k, l)] J(k, l) - \omega(i, j)\Gamma(i, j) \right)^2
\tag{7}
$$

where Γ represents the target image which is taken as the drawn mask in our simulation. Here, the simulated images are normalized to the range between 0 and 1. In addition, other elaborated target designs can also be applied to our formula [19], [41]. The weight function ω selects the images

locating on both inside and outside margins of drawn patterns. Moreover, the detecting points surrounding drawn patterns are included in ω to prevent undesired images (side-lobes) from being printed. Therefore, the weight function ω is defined as:

$$
\omega(i, j) = \begin{cases}
\rho_1, & \nabla_T m(i, j) \neq (0, 0) \text{ where} \\
& (i, j) \in \text{marginal points}, \\
\rho_2, & \nabla_T m(i \pm d_0, j \pm d_0) \neq (0, 0) \text{ where} \\
& (i, j) \in \text{side-lobe detecting points}, \\
0, & \text{otherwise}
\end{cases}
\tag{8}
$$

where ∇_T is a 2D gradient operator [43] that calculates the pixel differences along the direction of column (i) and row (j) and m is the spatial configuration of drawn patterns. d_0 is the index distance from the side-lobe detecting index to any edge index. ρ_1 and ρ_2 are the weighting coefficients of the marginal image and the side-lobe costs. $\nabla_T m(i, j)$ can be considered as an edge-detection function. In this design not only the image fidelity and side-lobes are considered, but also the image contrast is included because the sharp changes of drawn edges require high image contrasts in the optimization. Even if the weight assigned to the non-gradient portions is zero, the printing is still correct because the gradient of the target on the edge governs the trend of the image distribution. The image having same marginal value but reverse to the target is impossible for the sub-wavelength pattern images. As a result, Eq. (7) represents a line-contour objective function.

To simplify the matrix computation, the 2D discrete source J and the weighted target $\omega\Gamma$ can be converted to 1D vectors. The bracket in Eq. (7) can be replaced by a 2D matrix. Thus Eq. (7) can be rewritten as

$$
F_{Overall} = \left\| ICC' J - \Gamma' \right\|^2
\tag{9}
$$

where the sizes of $\mathbf{ICC'}$, $\mathbf{J}$, and Γ' are $N^2 \times O^2$, $O^2 \times 1$, and $N^2 \times 1$, respectively. Γ' is the sub-mask (corresponding to critical regions) target image converted to a 1D vector. $\|\cdot\|$ is the *Euclidean* norm.

By defining objective functions on the critical parts of the image and formulating the objective function as a quadratic operation, the computational cost of SO is significantly reduced.

C. Optimization for SO

In terms of matrix operations Eq. (7) can be rewritten as

$$
F_{Overall} = (ICC' J - \Gamma')^{\mathrm{T}}(ICC' J - \Gamma').
\tag{10}
$$

Consequently the optimal source $\hat{\mathbf{J}}$ can be defined as an argument for minimizing Eq. (10)

$$
\hat{\mathbf{J}} = \arg\min_{\mathbf{J}}\{F_{Overall}\}.
\tag{11}
$$

Moreover, Eq. (11) can be expanded to have a quadratic form

$$
F_{Overall} = J^{\mathrm{T}} Q J - b^{\mathrm{T}} J + c
\tag{12}
$$

where

$$
Q = ICC'^{\mathrm{T}} ICC'
\tag{13}
$$

$$
b = 2ICC^T \Gamma'
\tag{14}
$$

$$
c = \Gamma'^{\mathrm{T}} \Gamma'.
\tag{15}
$$

Algorithm 1 SO by CG

Input:

Load the initial source $\mathbf{J}^{(0)}$. Set $k = 0$.

Calculation:

1. $\mathbf{g}^{(0)} = \nabla_{\mathbf{J}} F_{\text{Overall}}(\mathbf{J}^{(0)})^{\dagger}$. If $\mathbf{g}^{(0)} < \varepsilon^{\ddagger}$, stop; else, set $\mathbf{d}^{(0)} = -\mathbf{g}^{(0)}$.
2. $\alpha_k = -(\mathbf{g}^{(k)T}\mathbf{d}^{(k)})/(\mathbf{d}^{(k)T}\mathbf{Q}\mathbf{d}^{(k)})$.
3. $\mathbf{J}^{(k+1)} = \mathbf{J}^{(k)} + \alpha_k \mathbf{d}^{(k)}$.
4. $\mathbf{g}^{(k+1)} = \nabla_{\mathbf{J}} F_{\text{Overall}}(\mathbf{J}^{(k+1)})$. If $\|\mathbf{g}^{(k+1)}\| < \varepsilon$, stop; Set $\hat{\mathbf{J}} = \mathbf{J}^{(k+1)}$.
5. $\beta_k = (\mathbf{g}^{(k+1)T}\mathbf{Q}\mathbf{d}^{(k)})/(\mathbf{d}^{(k)T}\mathbf{Q}\mathbf{d}^{(k)})$.
6. $\mathbf{d}^{(k+1)} = -\mathbf{g}^{(k+1)} + \beta_k \mathbf{d}^{(k)}$. Set $k = k + 1$; Go to step 2.

Output: Export the optimal source $\hat{\mathbf{J}}$.

$\dagger$ $\mathbf{g} = 2(\mathbf{Q}\mathbf{J} - \mathbf{b})$. $\nabla_{\mathbf{J}} = [\partial/\partial\mathbf{J}(1, 1), \partial/\partial\mathbf{J}(2, 1), \ldots, \partial/\partial\mathbf{J}(O, O)]^{\text{T}}$.

$\ddagger$ ε is an extremely small value.

The sizes of $\mathbf{Q}$, $\mathbf{b}$ and c are $O^2 \times O^2$, $O^2 \times 1$, and 1×1, respectively. Because the overall objective function is quadratic, the optimal source $\hat{\mathbf{J}}$ is guaranteed to be found with the conjugate-gradient (CG) method no more than O^2 iterative searching [44]. Although the minimum of a quadratic function can be found by a direct solver, its computational complexity is proportional to O^3 and is inferior to CG for large scale quadratic programming. The details of our implementation of CG are listed in Algorithm 1.

Because the computation of ICC is prohibitive for large-scale SO, we propose an innovative source synthesis method where the optimal source for a large mask is composed of the linearly superposed optimal sources of sub-masks:

$$J_{Syn.} = \hat{A}w \qquad (16)$$

where $\hat{\mathbf{A}} = [\hat{\mathbf{J}}_1, \hat{\mathbf{J}}_2, \ldots, \hat{\mathbf{J}}_L]$ represents optimal sources of sub-masks. $\mathbf{w} = [w_1, w_2, \ldots, w_L]^{\text{T}}$ stores the coefficients for synthesizing the optimal source $\mathbf{J}_{Syn.}$ for the large mask. L is the number of sources selected for synthesis. So the sizes of $\hat{\mathbf{A}}$ and $\mathbf{w}$ are $O^2 \times L$ and $L \times 1$, respectively. An analytic approach to obtain the proper value of $\mathbf{w}$ is the key to the success of source synthesis for large-scale SO. So far, the variable number is reduced from $O \times O$ source points to L coefficients. Such optimization can be quickly done in MO stage by using a few convolution kernels for OPC.

D. Synthesized Illumination via Linear Superposition of Optimal Sources

Our illumination synthesis is inspired by the Hopkins formulation for building the sum of coherent systems (SOCS) [34], [45], which allows a partially coherent image to be approximated by the convolution of a few eigenfunctions with the mask. The source synthesis is an overdetermined problem with the number of equations far exceeding the number of unknowns and can be solved as an LLS problem. With a few representative patterns on each mask layer, we can solve the weight coefficients using their pre-stored optimal sources in real time.

Using the sum of the optimal sources of sub-masks as an excitation, the transmission cross coefficient (TCC) of a partially coherent imaging system becomes [34], [45]:

$$TCC(f', g'; f'', g'') = \sum_{\iota=1}^{L} w_{\iota} \Bigg[\int_{-\infty}^{+\infty} \int \hat{J}_{\iota}(f, g)$$

$$\times H(f + f', g + g')H^*(f + f'', g + g'')df\,dg \Bigg]. \quad (17)$$

The bracket in Eq. (17) can be replaced by TCC_{ι} for a more succinct expression

$$TCC(f', g'; f'', g'') = \sum_{\iota=1}^{L} w_{\iota} TCC_{\iota}(f', g'; f'', g''). \quad (18)$$

Similarly to the derivation of SOCS, TCC_{ι} is approximated by dominant eigenfunctions as

$$I(i, j) = \sum_{\iota=1}^{L} w_{\iota} \left(\sum_{q=1}^{Q} \kappa_{\iota q} \left| (\phi_{\iota q} \otimes m)(i, j) \right|^2 \right)$$

$$= \sum_{\iota=1}^{L} w_{\iota} \hat{I}_{\iota}(i, j) \qquad (19)$$

where $\kappa_{\iota q}$ is the qth eigenvalue of the TCC_{ι} using the ιth source. $\phi_{\iota q}$ is the inverse Fourier transform of the eigenfunction, and $\hat{I}_{\iota}$ is the image distribution of the ιth source. Performing a matrix-to-vector conversion, we have

$$I = Aw \qquad (20)$$

where $\mathbf{A} = [\hat{\mathbf{I}}_1, \hat{\mathbf{I}}_2, \ldots, \hat{\mathbf{I}}_{\iota}, \ldots, \hat{\mathbf{I}}_L]$. The size of $\mathbf{A}$ and $\hat{\mathbf{I}}_{\iota}$ are $N^2 \times L$ and $L \times 1$, respectively. At this stage the overall cost can be expressed as

$$F_{Overall} = (\mathbf{A}'\mathbf{w} - \Gamma'_{\text{full}})^{\text{T}}(\mathbf{A}'\mathbf{w} - \Gamma'_{\text{full}}) \qquad (21)$$

where $\mathbf{A}' = [\omega \cdot \hat{\mathbf{I}}_1, \omega \cdot \hat{\mathbf{I}}_2, \ldots, \omega \cdot \hat{\mathbf{I}}_{\iota}, \ldots, \omega \cdot \hat{\mathbf{I}}_L]$, ω is the 1D weight map converted from ω in Eq. (7), while the operator $\cdot$ denotes the element-to-element multiplication. Γ'_{full} is the target image of the full mask. Eq. (21) can also be expanded to a quadratic form as Eq. (12)

$$F_{Overall} = w^{\text{T}} Q'w - b'^{\text{T}}w + c' \qquad (22)$$

where the sizes of $\mathbf{Q}'$, $\mathbf{b}'$, and c' are $L \times L$, $L \times 1$, and 1×1, respectively. $\mathbf{Q}'$, $\mathbf{b}'$, and c' have similar forms as Eqs. (13), (14), and (15), but $\mathbf{ICC}'$ is replaced by $\mathbf{A}'$ instead. In general the number of total image points N is much larger than the number of sources L. Therefore, the weighting coefficients for minimizing Eq. (22) can be written as

$$\hat{\mathbf{w}} = \mathbf{Q}'^{-1}\mathbf{b}' \qquad (23)$$

where the size of $\hat{\mathbf{w}}$ is $L \times 1$. The cost for computing $\mathbf{Q}'^{-1}$ is low because the number of sources L is small for the few sub-masks selected on a single layer. Fig. 3 summarizes the procedure for calculating the weighting coefficients $\hat{\mathbf{w}}$. Please note that the sources $\hat{\mathbf{J}}_1, \hat{\mathbf{J}}_2, \ldots, \hat{\mathbf{J}}_L$ are optimized for critical sub-masks but the coefficients $\hat{w}_1, \hat{w}_2, \ldots, \hat{w}_L$ are optimized for the full mask.
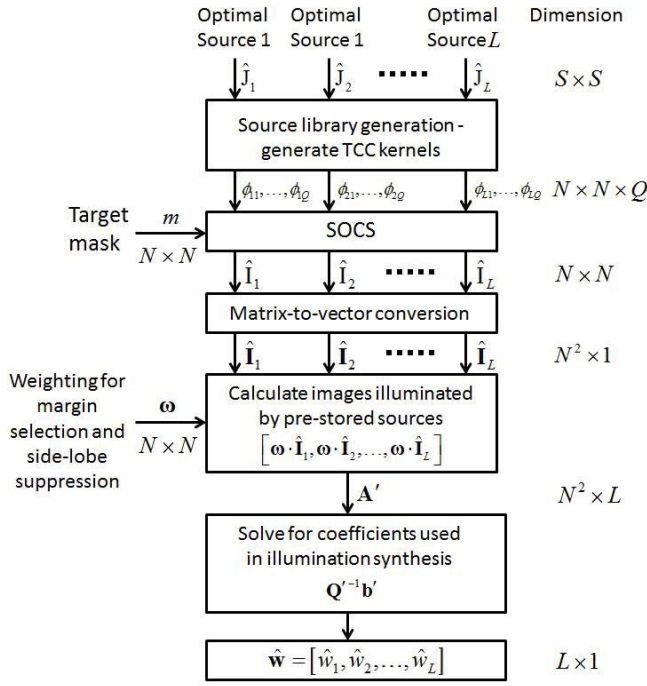
Fig. 3. Inputs, outputs, and control flow for calculating the coefficients used in illumination synthesis.

Fig. 4. Dissection of a rectangle into segments of equal length.

The synthesized *TCC* is readily available by switching the order of summation and integration in Eq. (17)

$$T\hat{C}C(f', g'; f'', g'') = \int_{-\infty}^{+\infty} \int \left(\sum_{l=1}^{L} \hat{w}_l \hat{J}_l(f, g) \right)$$
$$\times H(f + f', g + g') H^*(f + f'', g + g'') df dg. \quad (24)$$

Hence the discrete aerial image can be re-written as

$$I(i, j) = \sum_{q=1}^{Q} \kappa'_q \left| (\phi'_q \otimes m)(i, j) \right|^2 = \sum_{q=1}^{Q} \left| \hat{E}_q(i, j) \right|^2 \quad (25)$$

where κ'_q is the qth eigenvalue of the $T\hat{C}C$, ϕ'_q is the inverse Fourier transform of the eigenfunction, and $\hat{E}_q$ is the electrical field contributed by the qth eigenfunction.

E. Model-Based OPC for MO

Even though the subject of our paper is illumination synthesis, the resolution enhancement process would not be complete without MO. In Section III we will see the advantage of a synthesized source over a conventional one in alleviating the constraints in MO.

Our MO is based on a segment-based OPC [45], [46], which starts by dissecting drawn pattern edges to connected segments (Fig. 4).
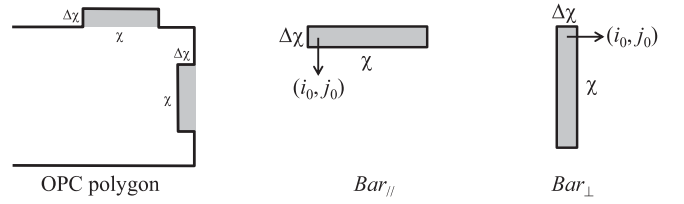

Fig. 5. Horizontal and vertical bars formed by offsetting segments in a polygon, where χ is the segment length and $\Delta\chi$ is the offset distance. (i, j) denotes the pixel indices.

Then look-up tables are generated by vertex-based techniques as the patterns are Manhattan polygons [34], [45]. To further speed up MO, we propose a bar spread function (BSF) for evaluating field variation due to segment offsets. Such approach pre-calculates the convolution associated with horizontal and vertical bars whose areas are equal to the segment lengths multiplied by the offsets. Fig. 5 illustrates the terminal of an OPC polygon and corresponding horizontal $(Bar_{//})$ and vertical $(Bar_{\perp})$ bars.

The BSFs of horizontal and vertical bars can be written as

$$\begin{cases} \psi_{//q}(i, j) = (Bar_{//} \otimes \hat{\phi}_q)(i, j), \\ \psi_{\perp q}(i, j) = (Bar_{\perp} \otimes \hat{\phi}_q)(i, j) \end{cases} \quad (26)$$

and their contribution to the electrical fields of all kernels is

$$\Delta\hat{E}_q^{(n)}(i, j) =$$
$$\begin{cases} \psi_{//q}(i_0^{(n)} - i, j_0^{(n)} - j), & \text{if } n^{th} \text{ segment is horizontal} \\ \psi_{\perp q}(i_0^{(n)} - i, j_0^{(n)} - j), & \text{if } n^{th} \text{ segment is vertical.} \end{cases} \quad (27)$$

The aerial image after offsetting n^{th} segment is

$$I^{\Delta(n)} = \sum_{q=1}^{Q} \left| \hat{E}_q(i, j) \pm \Delta\hat{E}_q^{(n)}(i, j) \right|^2 \quad (28)$$

where $\pm$ denotes the segments being shifted outward$(+)$ or inward$(-)$. Using BSF-based field updates, we gain a speedup of four (36 versus 144 minutes on Intel Xeon E5420 at 2.50 GHz) compared with the conventional method [34], [45].

To evaluate the quality of aerial images, the objective function is designed for quantifying image fidelity, image contrast and side-lobe printing:

$$F_{Overall} = (\omega \cdot I^{\Delta(n)} - \Gamma')^{\mathrm{T}}(\omega \cdot I^{\Delta(n)} - \Gamma') \quad (29)$$

where $\mathbf{I}^{\Delta(n)}$ is an $N \times 1$ vector representing 1D aerial images of their 2D counterparts in Eq. (28). Therefore, the image qualities are evaluated by Eq. (29) depending on whether the segments are shifted in, out, or neither.

III. RESULTS

Our simulations assume partially coherent illumination with $\lambda = 193$ nm, $NA = 1.35$, and $\sigma = 0.9$. The pixel resolutions in source and mask templates are 1.97×10^{-4} nm^{-1} and 2.48 nm, respectively. The coordinates of source templates are normalized by $\sigma NA/\lambda$ and the images are normalized to have unit intensity. For all simulations in Section III, the weighting coefficients ρ_1 and ρ_2 in Eq. (8) are chosen to be the inverses of the perimeters of drawn patterns and side-lobe monitor
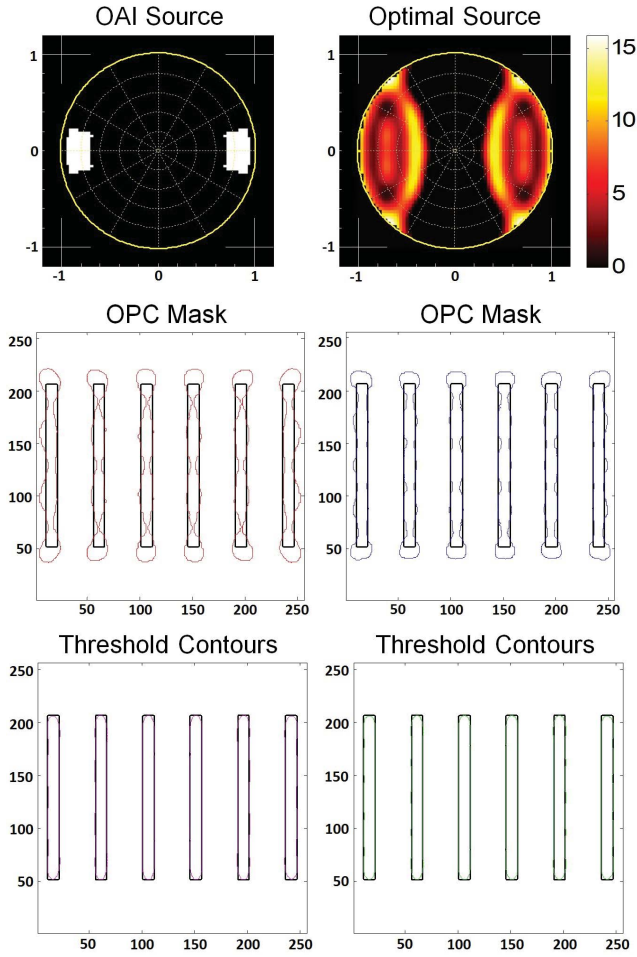
Fig. 6. Comparisons of the OPC masks and related threshold contours using OAI and optimal sources, respectively.
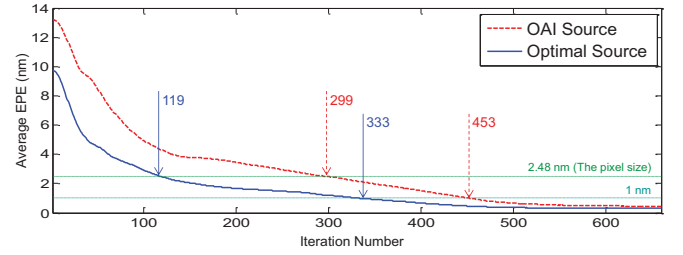

Fig. 7. Dashed line: convergence of EPEs exposed by OAI. Solid line: optimal sources.

TABLE I
COMPARISONS OF THE OAI AND OPTIMAL SOURCES FOR ILLUMINATIONS

Metrics Compares	Mask Edge Number	Average EPE (nm)	Iterations Number	
			Average EPE < Pixel Size	Average EPE < 1 nm
OAI	1176	0.45	299	453
Optimal source	960	0.32	119	333
Improvement (%)	18.37	28.89	48.03	26.49

rings, respectively. Such setting of weighting coefficients ρ_1 and ρ_2 is mainly used to equalize the importance of getting an ideal marginal image and suppressing the side-lobes during optimization.

A. Comparison of OAI and Optimal Freeform Sources

We first compare a conventional OAI source empirically chosen for a mask composed of a vertical line array (256 × 256 pixels), which has a CD and a pitch of 27.3 nm and 111.7 nm, respectively. The chosen dimensions are very challenging for 193 nm optical emersion lithography without the assistance of double patterning and phase shifting masks. As shown in Fig. 6, an optimized binary dipole source is used as the reference in which the inner and outer radii are set to be 0.7 and 0.95 with a total intensity equal to 50.84. In contrast, the calculated optimal source also has a dipole form with an extended intensity distribution.

Fig. 6 further shows the OPC masks in red and blue edges, as well as the corresponding threshold contours of the aerial images calculated based on the optimized OAI and freeform sources, respectively. Compared to the drawn masks in black solid lines, the optimal freeform source helps to reduce the mask edges of the vertical line array by 18.37%

and improves the image fidelity as the average edge placement error (EPE) also decreases by 28.89%. The results indicate that the complexity of masks correction can be relieved by means of an optimized freeform source.

Moreover, illuminating by the optimal source also speeds up the OPC calculation, which is shown in Fig. 7. The average EPE is below pixel size after 119 iterations as using the optimal source while the 229 iterations are required as illuminating by OAI. Such efficiency improvement is about 48.03%. Then, it improves 26.49% from 453 to 333 iterations to attain the 1 nm average EPE. The convergence below 0.5 nm EPE well satisfies the current CD requirement in 193 nm optical lithography even at the 20 nm process node. The saturation of the convergence rate in Fig. 7 also implies that both OAI and freeform sources nearly reach the global minimum. Therefore, for the examples studied in the paper, we observed only marginal improvement when the synthesized source was fed to an iterative SMO (Fig. 2) beyond two iterations. To demonstrate the sole effect of the synthesized source and isolate it from the complication of iterative SMO, here we mainly present the results obtained from single-pass separated SMO. Table I summarizes the above comparisons where the optimal source presents promising results that promote the use of synthesized sources for full mask source optimization.

B. Library-Based Source Synthesis and Comparison

Next, three sub-masks (256 × 256 pixels) of poly structures including a vertical line array, a horizontal line array, and a brick array are employed. The dimensions of each sub-mask are indicated in Fig. 8. As mentioned before, the choice of 27.3 nm critical dimension (CD) in these test cases is very challenging for current optical lithography without other reticle enhancement techniques. The optimal sources (64 × 64 pixels) for individual patterns are then precalculated and stored in a library. Thus L is equal to 3.
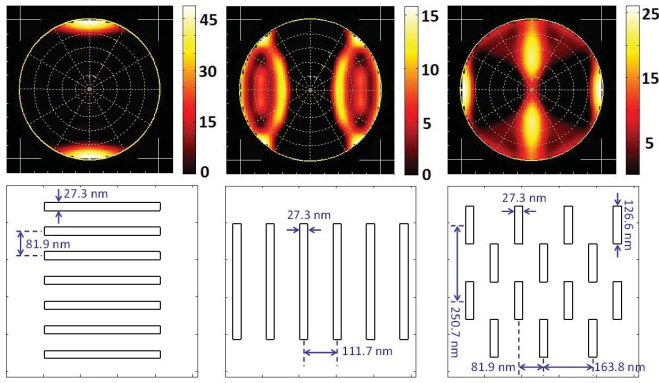
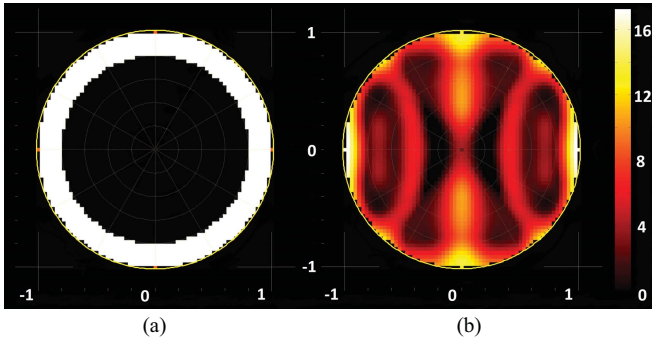Fig. 8. Submasks and corresponding optimal sources.
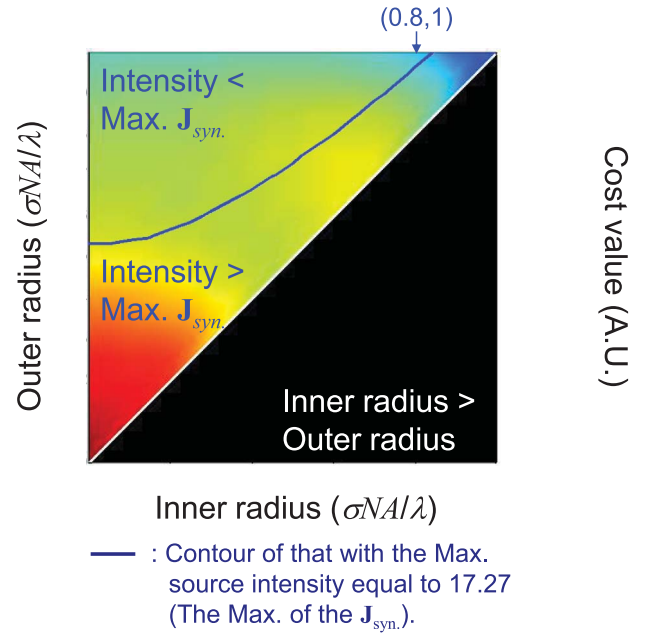

Fig. 9. (a) Annular and (b) synthesized sources.

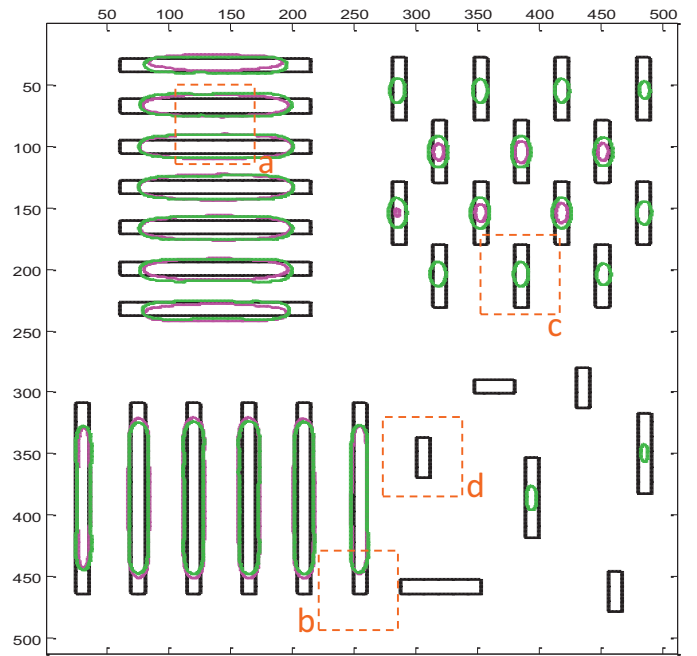Fig. 10. Cost map of annular sources with varying inner and outer radii.

Fig. 11. Aerial images of the non-OPC mask exposed by annular and synthesized sources. Orange dashed rectangles: critical regions of individual submasks.

To demonstrate the advantage of synthesized illumination, three sub-masks are tied together to form a large mask. By applying Eq. (23), we determine the analytic coefficients for synthesizing the optimal source to be 0.19, 0.57, and 0.39, respectively, for the sources from left to right in Fig. 8. The synthesized source is plotted in Fig. 9. Moreover, since the sub-masks contain vertical and horizontal line arrays, as well as alternatively arranged brick patterns, the conventional binary source is chosen to be annual for best image fidelity.

To make the total energy of the two sources equivalent for fair comparison, the intensity of the annular source is fine-tuned for the energy conservation. Moreover, the annular sources with the intensity over the maximum of the synthesized source are discarded to prevent damages due to overheated metal parts on the mask. Fig. 10 illustrates the cost map of the annular source. Two variables, inner and outer normalized radii, vary from 0 to 1. The colors denote various values of the cost function in Eq. (7). We note that the annular source has been optimized for the best quality of aerial images to have an inner radius 0.80 and an outer radius 1.00. As a result, the intensity of the annular source is set to be 13.55.

To check the applicability of a synthesized source based on a pre-stored library to other patterns, randomly distributed polys with CD = 27.3 nm are added to pose more challenges. Obviously the new mask pattern has not been used for finding an optimal source in the source library. Therefore, there is no weighting coefficient associated with the pattern for illumination synthesis. This happens quite often in source planning for future technology nodes in semiconductor

foundries and original design manufacturers (ODMs). Critical patterns such as contacts and vias with stringent CDs are first studied for planning the source requirement and design rules. After entering the circuit design phase or customers submit their layouts, more comprehensive full-chip SMO has to be conducted for post-layout OPC. In this paper we position the illumination synthesis to address the need of fast source prototyping during pre-layout path-finding before the less critical layouts are available.

In Fig. 11 the black, magenta, and green contours represent drawn mask edges, image contours of the annular source,
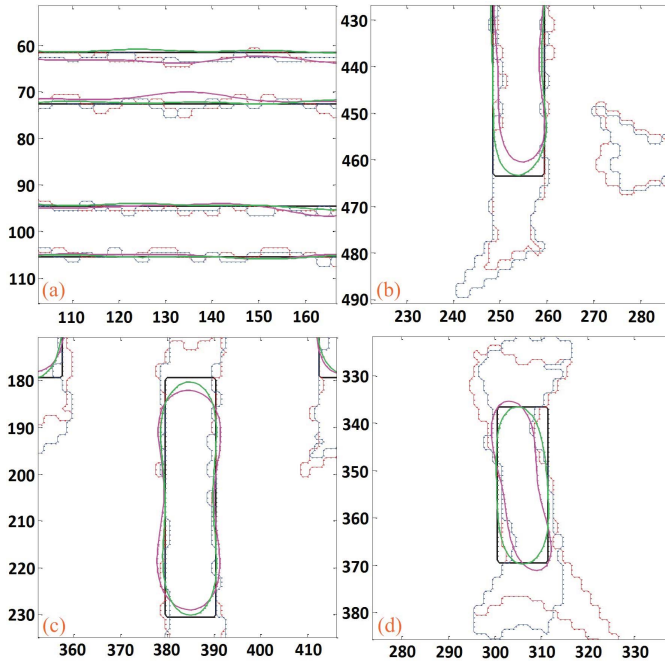
Fig. 12. MB-OPC masks and post MB-OPC image contours associated with annular and synthesized illumination. (a)–(d) Eight times zoom of the critical regions in Fig. 11.
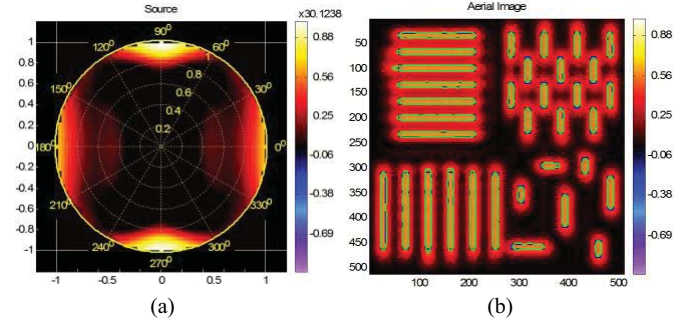

Fig. 13. (a) Source Optimized by iterative SMO [40] with the full mask in Fig. 11 and (b) its associated aerial image after MB-OPC.

Fig. 14. Locations of CD cut lines for long and short polys.

TABLE II

AVERAGE EPE (nm) AND NILS (AU) FOR MB-OPC MASKS EXPOSED BY ANNULAR, SYNTHESIZED, AND FULL-MASK-OPTIMIZED SOURCES

Patterns		Horizontal Line Array	Vertical Line Array	Brick Ploy Array	Random Ploys	Full Mask
Pitch (nm)		81.9	111.7	(81.9, 163.8)	–	–
CD: Pitch		1:3	1:4	1:3; 1:6	–	–
Annular	EPE	1.24	0.63	1.24	0.81	1.03
	NILS	0.28	0.43	0.80	0.66	0.56
Synthesized	EPE	0.31	0.21	0.48	0.46	0.37
	NILS	0.38	0.48	0.80	0.69	0.60
Source optimized by full mask	EPE	0.23	0.38	0.31	0.34	0.31
	NILS	0.47	0.44	0.39	0.35	0.42

and image contours of the synthesized source, respectively. Although the image contours of both sources differ quite a lot from the drawn mask edges, it is not a big concern because the difference will later be eliminated by model-based (MB) OPC in MO. Even without MO, the synthesized source already demonstrates its advantage of printing more patterns than the annular source.

C. Evaluation After SMO

In terms of MO two MB-OPC runs are performed under annular and synthesized illumination. The segment length χ and its displacement $\Delta\chi$ are set to 7.45 nm and 2.48 nm

respectively. In order to generate manufacturing friendly masks, the cliff of any two adjacent segments should not exceed $3\Delta\chi$ (7.45 nm). Fig. 12 shows the image contours of the critical regions in Fig. 11. The black curves are drawn pattern edges. Red and blue curves are the edges of the MB-OPC masks associated with annular and synthesized sources, while the magenta and green curves are the image contours associated with annular and synthesized sources.

Table II confirms that both EPE and normalized image log slopes (NILS) are indeed better for synthesized illumination. The quality of the images is better not only for individual sub-masks, but also for the full mask. Although the green contours do not align with the drawn mask edges well near line endings in the critical region a, their EPEs are acceptable because they are under 1.25 nm ($\Delta\chi/2$), which is less than $\Delta\chi$.

Generally speaking, the mask correction for the synthesized illumination is less aggressive than that of the conventional counterpart, which is an indication of the better choice of illumination source. EPE is improved more than NILS because OPC is inherent for correcting to pattern fidelity. Although the contrast is embedded in the objective functions, it is improved as a side benefit of OPC.

To further check the optimality of the synthesized source, we perform iterative SMO [40] to find the optimized source (Fig. 13) for the entire mask (Fig. 11) which includes both critical and non-critical patterns. As shown in Table II, the full-mask-optimized source may have smaller EPE and larger NILS than the synthesized source. But it is not true for all the cases. The synthesized source provides an initial solution which is close to optimal for a single-pass separated SMO. However, the iterative SMO in [40] may not be able to reach the optimal solution if being fed with an arbitrary initial guess. The NILS of the full-mask-optimized source is generally smaller than that of the synthesized source in Table II.

In addition to the image quality being evaluated by EPE and NILS, we also evaluate the process variation by the exposure-defocus process window (E-D PW) for annular and synthesized sources. The CD cut lines for measuring E-D PWs are shown in Fig. 14 for long (in line array) and short (in brick array and random placement) polys.
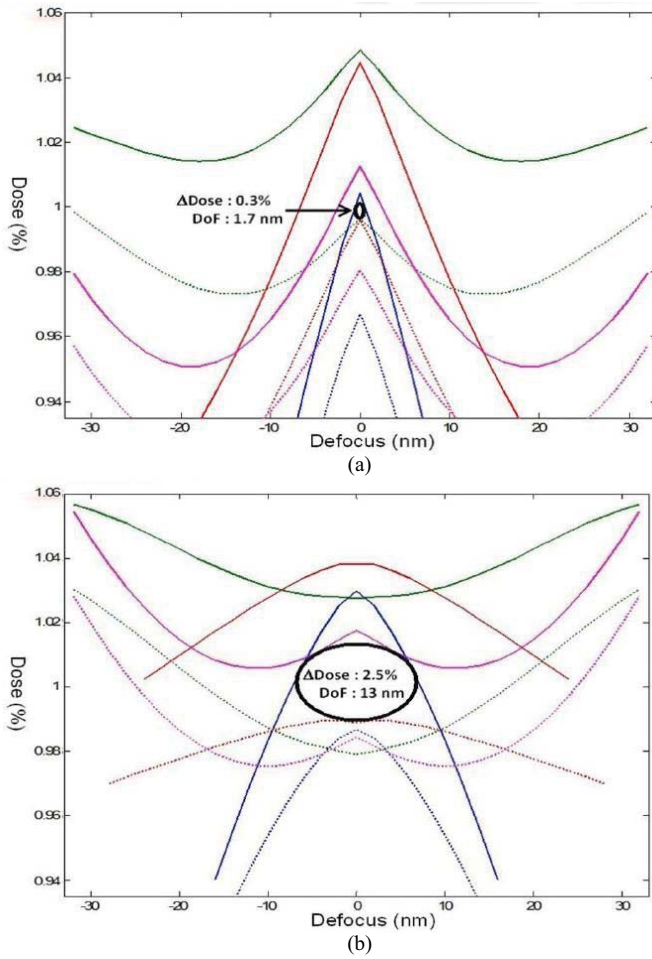
Fig. 15. (a) E-D PWs of MO with the annular source. (b) SMO with the synthesized source.

TABLE III
DOSE (%) AND DoF (nm) FOR MB-OPC MASK EXPOSED BY
ANNULAR AND SYNTHESIZED SOURCES

Patterns		Horizontal Line Array	Vertical Line Array	Brick Ploy Array	Random Ploys	Full Mask
Pitch (nm)		81.9	111.7	(81.9, 163.8)	–	–
CD: Pitch		1:3	1:4	1:3; 1:6	–	–
Annular	**ΔDose**	2.0	3.0	4.0	2.3	0.3
	DoF	3.84	26.32	7.31	6.72	1.70
Synthesized	**ΔDose**	3.5	3.6	3.0	2.4	2.5
	DoF	10.67	41.30	42.40	46.30	13.00

Fig. 15 shows the E-D PWs of the experiments that use the post corrected masks under annular and synthesized illumination. The solid and dashed lines denote the CD+10% and CD−10% bias E-D curves, respectively. The blue, green, red, and magenta are CD curves of the horizontal line array, the vertical line array, the brick poly array, and the random polys, respectively. Obviously the synthesized source with its MB-OPC mask tolerates larger process variation than the annular source with its MB-OPC mask. For a detailed comparison, we tabulate the maximum acceptable dose deviation (ΔDose) and the depth of focus (DoF) of individual sub-

masks and the full mask (Table III). We believe that the high contrast images resulting from SO provide extra budget to overcome the image degradation from defocus aberrations due to positioning errors.

IV. CONCLUSION

In this paper, we propose a library-based approach for illumination synthesis by using the superposition of pre-stored optimized sources from sub-cells representing full-chip characteristics. A rigorous algorithm is developed by first formulating SO into a quadratic programming problem with the introduction of line-contour objective functions. Then the weighting coefficients for source superposition can be solved exactly via Hopkins formulation and linear programming. As a proof of concept, we further demonstrate that the synthesized source enhances the pattern fidelity and process window over its annular counterpart with conventional segment-based optical proximity correction. This novel approach mitigates aggressive reticle modification by shifting the complexity of masks to illumination sources, and therefore is fully compatible with existing RET options in current manufacturing flows. The low computational complexity also makes our approach especially favorable for large-scale SMO.

REFERENCES

[1] B. J. Lin, *Optical Lithography: Here is Why*. Bellingham, WA, USA: SPIE, 2010.
[2] S. Sherif, B. Saleh, and R. Leone, "Binary image synthesis using mixed linear integer programming," *IEEE Trans. Image Process.*, vol. 4, no. 9, pp. 1252–1257, Sep. 1995.
[3] L. Pang, Y. Liu, and D. Abrams, "Inverse lithography technology (ILT): What is the impact to the photomask industry?" *Proc. SPIE*, vol. 6283, pp. 62830X-1–62830X-11, Apr. 2006.
[4] A. Poonawala and P. Milanfar, "Mask design for optical microlithography—An inverse imaging problem," *IEEE Trans. Image Process.*, vol. 16, no. 3, pp. 774–788, Mar. 2007.
[5] X. Ma and G. R. Arce, "Generalized inverse lithography methods for phase-shifting mask design," *Opt. Exp.*, vol. 15, no. 23, pp. 15066–15079, Nov. 2007.
[6] X. Ma and G. R. Arce, "PSM design for inverse lithography with partially coherent illumination," *Opt. Exp.*, vol. 16, no. 24, pp. 20126–20141, Nov. 2008.
[7] X. Ma and G. R. Arce, "Binary mask optimization for inverse lithography with partially coherent illumination," *J. Opt. Soc. America A*, vol. 25, no. 12, pp. 2960–2970, Dec. 2008.
[8] X. Ma and G. R. Arce, "Pixel-based OPC optimization based on conjugate gradients," *Opt. Exp.*, vol. 19, no. 3, pp. 2165–2180, Jan. 2011.
[9] X. Ma, Y. Li, and L. Dong, "Mask optimization approaches in optical lithography based on a vector imaging model," *J. Opt. Soc. America A*, vol. 29, no. 7, pp. 1300–1312, Jul. 2012.
[10] Y. Shen, N. Jia, N. Wong, and E. Y. Lam, "Robust level-set-based inverse lithography," *Opt. Exp.*, vol. 19, no. 6, pp. 5511–5521, Mar. 2011.
[11] A. Poonawala, Y. Borodovsky, and P. Milanfar, "ILT for double exposure lithography with conventional and novel materials," *Proc. SPIE*, vol. 6520, pp. 65202Q-1–65202Q-14, Mar. 2007.
[12] K. Lucas, C. Cork, A. Miloslavsky, G. L. Pat, L. Barnes, J. Hapli, J. Lewellen, G. Rollins, V. Wiaux, and S. Verhaegen, "Double-patterning interactions with wafer processing, optical proximity correction, and physical design flows," *J. Micro/Nanolithogr., MEMS, MOEMS*, vol. 8, no. 3, pp. 033002-1–033002-10, Jul.–Sep. 2009.

[13] T. Dam, R. Sinn, P. Rissman, and B. Gleason, "Exploring the impact of mask making constraints on double patterning design rules," *Proc. SPIE*, vol. 8166, pp. 816629-1–816629-11, Oct. 2011.

[14] X. Ma and G. R. Arce, "Pixel-based simultaneous source and mask optimization for resolution enhancement in optical lithography," *Opt. Exp.*, vol. 17, no. 7, pp. 5783–5793, Mar. 2009.

[15] N. Jia and E. Y. Lam, "Pixelated source mask optimization for process robustness in optical lithography," *Opt. Exp.*, vol. 19, no. 20, pp. 19384–19398, Sep. 2011.

[16] Y. Peng, J. Zhang, Y. Wang, and Z. Yu, "Gradient-based source and mask optimization in optical lithography," *IEEE Trans. Image Process.*, vol. 20, no. 10, pp. 2856–2864, Oct. 2011.

[17] J. Li, Y. Shen, and E. Y. Lam, "Hotspot-aware fast source and mask optimization," *Opt. Exp.*, vol. 20, no. 19, pp. 21792–21804, Sep. 2012.

[18] A. E. Rosenbluth, S. Bukofsky, C. Fonseca, M. Hibbs, K. Lai, A. Molless, R. N. Singh, and A. K. K. Wong, "Optimum mask and source patterns to print a given shape," *J. Micro/Nanolithogr., MEMS, MOEMS*, vol. 1, no. 1, pp. 13–30, Apr. 2002.

[19] Y. Granik, "Source optimization for image fidelity and throughput," *J. Micro/Nanolithogr., MEMS, MOEMS*, vol. 3, no. 4, pp. 509–522, Oct. 2004.

[20] R. Socha, X. Shi, and D. LeHoty, "Simultaneous source mask optimization (SMO)," *Proc. SPIE*, vol. 5853, pp. 180–193, Jun. 2005.

[21] K. Iwase, P. D. Bisschop, B. Laenens, Z. Li, K. Gronlund, P. V. Adrichem, and S. Hsu, "A new source optimization approach for 2X node logic," *Proc. SPIE*, vol. 8166, pp. 81662A-1–81662A-11, Oct. 2011.

[22] Y. Deng, Y. Zou, K. Yoshimoto, Y. Ma, C. E. Tabery, J. Kye, L. Capodieci, and H. J. Levinson, "Considerations in source-mask optimization for logic applications," *Proc. SPIE*, vol. 7640, pp. 76401J-1–76401J-12, Mar. 2010.

[23] T. Mülders, V. Domnenko, B. Küchler, T. Klimpel, H. J. Stock, A. A. Poonawala, K. N. Taravade, and W. A. Stanton, "Simultaneous source-mask optimization: A numerical combining method," *Proc. SPIE*, vol. 7823, pp. 78233X-1–78233X-12, Sep. 2010.

[24] K. Tian, A. Krasnoperova, D. Melville, A. E. Rosenbluth, D. Gil, J. T. Azpiroz, K. Lai, S. Bagheri, C. C. Chen, and B. Morgenfeld, "Benefits and trade-offs of global source optimization in optical lithography," *Proc. SPIE*, vol. 7274, pp. 72740C-1–72740C-12, Mar. 2009.

[25] J. Bekaert, B. Laenens, S. Verhaegen, L. Van Look, D. Trivkovic, F. Lazzarino, G. Vandenberghe, P. van Adrichem, R. Socha, S. Baron, M. C. Tsai, K. Ning, S. Hsu, H. Y. Liu, M. Mulder, A. Bouma, E. van der Heijden, O. Mouraille, K. Schreel, J. Finders, M. Dusa, J. Zimmermann, P. Gräupner, J. T. Neumann, and C. Hennerkes, "Freeform illumination sources: An experimental study of source-mask optimization for 22-nm SRAM cells," *Proc. SPIE*, vol. 7640, pp. 764008-1–764008-12, Mar. 2010.

[26] T. Dam, V. Tolani, P. Hu, K.-H. Baik, L. Pang, B. Gleason, S. D. Slonaker, and J. K. Tyminski, "Source-mask optimization (SMO): From theory to practice," *Proc. SPIE*, vol. 7640, pp. 764028-1–764028-10, Mar. 2010.

[27] I. Torunoglu, E. Elsen, and A. Karakas, "A GPU-based full-chip source-mask optimization solution," *Proc. SPIE*, vol. 7640, pp. 76401L-1–76401L-10, Mar. 2010.

[28] K. Lai, M. Gabrani, D. Demaris, N. Casati, A. Torres, S. Sarkar, P. Strenski, S. Bagheri, D. Scarpazza, A. E. Rosenbluth, D. O. Melville, A. Wächter, J. Lee, V. Austel, M. Szeto-Millstone, K. Tian, F. Barahona, T. Inoue, and M. Sakamoto, "Design specific joint optimization of masks and sources on a very large scale," *Proc. SPIE*, vol. 7973, pp. 797308-1–797308-13, Apr. 2011.

[29] M.-C. Tsai, S. Hsu, L. Chen, Y.-W. Lu, J. Li, F. Chen, H. Chen, J. Tao, B.-D. Chen, H. Feng, W. Wong, W. Yuan, X. Li, Z. Li, L. Li, R. Dover, H.-Y. Liu, and J. Koonmen, "Full-chip source and mask optimization," *Proc. SPIE*, vol. 7973, pp. 79730A-1–79730A-11, Mar. 2011.

[30] Y. Deng, T. H. Coskun, J. Kye, and H. J. Levinson, "Lithography target optimization with source-mask optimization," *Proc. SPIE*, vol. 8326, pp. 83262P-1–83262P-8, Feb. 2012.

[31] D. Zhang, G. Chua, Y. Foong, Y. Zou, S. Hsu, S. Baron, M. Feng, H.-Y. Liu, Z. Li, S. Jessy, T. Yun, C. Babcock, B. I. L. Choi, R. Stefan, A. Vavarra, T. Fischer, A. Leschok, X. Liu, W. Shi, J. Qiu, and R. Dover, "Source mask optimization methodology (SMO) and application to real full chip optical proximity correction," *Proc. SPIE*, vol. 8326, pp. 83261V-1–83261V-11, Feb. 2012.

[32] A. K. Wong, *Resolution Enhancement Techniques in Optical Lithography*. Bellingham, WA, USA: SPIE, 2001.

[33] F. M. Schellenberg, *Selected Papers on Resolution Enhancement Techniques in Optical Lithography*. Bellingham, WA, USA: SPIE, 2004.

[34] A. K. Wong, *Optical Imaging in Projection Microlithography*. Bellingham, WA, USA: SPIE, 2005.

[35] C. Mack, *Fundamental Principles of Optical Lithography: The Science of Microfabrication*. New York, NY, USA: Wiley, 2007.

[36] E. Y. Lam and A. K. Wong, "Computational lithography: Virtual reality and virtual virtuality," *Opt. Exp.*, vol. 17, no. 15, pp. 12259–12268, Jul. 2009.

[37] X. Ma and G. R. Arce, *Computational Lithography*. New York, NY, USA: Wiley, 2010.

[38] M. Born and E. Wolf, *Principles of Optics: Electromagnetic Theory of Propagation, Interference and Diffraction of Light*, 7th ed. Cambridge, U.K.: Cambridge Univ. Press, 1999.

[39] J. W. Goodman, *Introduction to Fourier Optics*, 3rd ed. Englewood, CO, USA: Roberts & Company Publishers, 2004.

[40] J. C. Yu and P. Yu, "Gradient-based fast source mask optimization (SMO)," *Proc. SPIE*, vol. 7973, pp. 797320-1–797320-13, Mar. 2011.

[41] J. C. Yu, P. Yu, and H. Y. Chao, "Wavefront-based pixel inversion algorithm for generation of subresolution assist features," *J. Micro/Nanolithogr., MEMS, MOEMS*, vol. 10, no. 4, pp. 043014-1–043014-12, Oct.–Dec. 2011.

[42] J. C. Yu, P. Yu, and H. Y. Chao, "Fast source optimization involving quadratic line-contour objectives for the resist image," *Opt. Exp.*, vol. 20, no. 7, pp. 8161–8174, Mar. 2012.

[43] R. C. Gonzalez and R. E. Woods, *Digital Image Processing*, 3rd ed. Upper Saddle River, NJ, USA: Prentice-Hall, 2007.

[44] E. K. P. Chong and S. H. Zak, *An Introduction to Optimization*, 3rd ed. New York, NY, USA: Wiley, 2008.

[45] N. B. Cobb, "Fast optical and process proximity correction algorithms for integrated circuit manufacturing," Ph.D. dissertation, Dept. Electr. Eng. Comput. Sci., Univ. California at Berkeley, Berkeley, CA, USA, 1998.

[46] P. Yu, S. X. Shi, and D. Z. Pan, "Process variation aware OPC with variational lithography modeling," *Proc. Design Autom. Conf.*, Jul. 2006, pp. 785–790.

Jue-Chin Yu received the B.S.E.E. degree from the Department of Electrical Engineering, National University of Kaohsiung, Kaohsiung, Taiwan, the M.S. degree from the Institute of Photonic Technologies, National Tsing Hua University, Hsinchu, Taiwan, and the Ph.D. degree from the Institute of Electro-Optical Engineering, National Chiao Tung University, Hsinchu, in 2004, 2006, and 2012, respectively.

He was an RET Engineering Intern at TSMC, Hsinchu, from 2009 to 2010. His current research interests include inverse problem of RET for 32 nm lithography and beyond, which includes inverse lithography and source-mask optimization.

Dr. Yu was a recipient of the Best Student Paper Awards in SPIE Lithography Asia 2008 and SPIE Advanced Lithography 2010, and the Lam Thesis Award in 2012.

Peichen Yu received the Ph.D. degree in electrical engineering from the University of Michigan, Ann Arbor, MI, USA, in 2004.

She was an RET Design Engineer with the Advanced Design Group, Intel Corporation, Hillsboro, OR, USA, from 2004 to 2006. In 2006, she joined the Department of Photonics and the Institute of Electro-Optical Engineering, National Chiao Tung University, as an Assistant Professor and was promoted to Associate Professor in 2009. She is also actively engaged in the development of OPC and DFM solutions for CMOS 32 nm microlithography and beyond. She has published over 40 refereed technical papers in the above research areas. Her work has been selected for Virtual Journal of Nanoscale Science & Technology and highlighted by SPIE newsroom, NPG Nature Asia-Material. Her current research interests include the design and development of nanostructured solar cells and light emitting diodes.

Dr. Yu is a member of the IEEE Photonics Society and SPIE.

Hsueh-Yung Chao received the B.S. degree from National Sun Yat-Sen University, Kaohsiung, Taiwan, in 1994, and the M.S. and Ph.D. degrees from the University of Illinois at Urbana-Champaign, Urbana, IL, USA, in 1998 and 2002, respectively.

He was a Research Assistant with the Center for Computational Electromagnetics, University of Illinois at Urbana-Champaign, from August 1996 to December 2002. From 1999 to 2002, he held summer internships with Intel Corporation, Hillsboro, OR, USA, where in 2003, he was a Senior CAD Engineer with the TCAD Department. In February 2004, he joined the Department of Communication Engineering, National Chiao Tung University, Hsinchu, Taiwan, as an Assistant professor. From September 2008 to May 2011, he was a Senior R&D Engineer at Synopsys, Mountain View, CA, USA, in electromagnetic simulation of optoelectronic devices. From 2011, he was a Lead R&D Engineer at ANSYS, Pittsburgh, PA, USA, on GPU acceleration of transient electromagnetic simulation. His current research interests include computational electromagnetics, optical imaging in microlithography, multiphysics simulation, and parallel computing.

Dr. Caho was a recipient of the Spontaneous Recognition Award from Intel in 2003 and the Excellence in Teamwork Award from Synopsys in 2009.